Lattice Boltzmann method for simulation of wettable particles at a fluid-fluid interface under gravity

Yasushi Mino [1] and Hiroyuki Shinto [2]

[1] *Division of Applied Chemistry, Graduate School of Natural Science and Technology, Okayama University, 3-1-1 Tsushima-naka, Kita-ku, Okayama 700–8530, Japan*

[2] *Department of Chemical Engineering, Fukuoka University, 8-19-1 Nanakuma, Jonan-ku, Fukuoka 814-0180, Japan*

(Received 26 September 2019; accepted 15 February 2020; published 13 March 2020)

A computational technique was developed to simulate wettable particles trapped at a fluid-fluid interface under gravity. The proposed technique combines the improved smoothed profile-lattice Boltzmann method (iSP-LBM) for the treatment of moving solid-fluid boundaries and the free-energy LBM for the description of isodensity immiscible two-phase flows. We considered five benchmark problems in two-dimensional systems, including a stationary drop, a wettable particle trapped at a fluid-fluid interface in the absence or presence of gravity, two freely moving particles at a fluid-fluid interface in the presence of gravity (i.e., capillary floatation forces), and two vertically constrained particles at a fluid-fluid interface (i.e., capillary immersion forces). The simulation results agreed well with theoretical estimations, demonstrating the efficacy of the proposed technique.

DOI: 10.1103/PhysRevE.101.033304

I. INTRODUCTION

Particles trapped at fluid-fluid interfaces of two-phase fluids are frequently observed in many natural phenomena and industrial processes, such as interfacial self-assembly [1–3], suppression of the coffee-ring effect [4], and capillary suspension [5]. Because particles captured at the fluid-fluid interfaces exhibit a variety of behaviors, the precise prediction and control of their motion are challenging problems. To gain a deeper understanding of the interfacial dynamics of particles, a numerical simulation has attracted significant interest as a promising approach.

In the numerical simulation of particle dynamics at fluid-fluid interfaces, one must handle a moving solid-fluid boundary in a two-phase fluid (fluid-fluid) system efficiently and accurately. A number of numerical simulation methods have been proposed for both solid-fluid systems [6–10] and fluid-fluid systems [11–16] within the framework of the lattice Boltzmann method (LBM) [17,18], which is a computational fluid dynamics solver used in this study. It is essential to select appropriate solid-fluid and fluid-fluid simulation methods for a target system and couple such methods efficiently. Therefore, various types of coupling methods have been developed, and new methods continue to be studied [19–22].

We recently reported a solid-fluid simulation method based on the smoothed profile (SP) method for the LBM solver [23], which is referred to as the improved SP-LBM (iSP-LBM) [24]. The iSP-LBM improved the accuracy and stability of the original SP-LBM by implementing an exact formulation for the hydrodynamic forces on a moving solid particle with consideration for the effects of internal fluid mass. In this study, we coupled the iSP-LBM with a two-phase LBM to develop a simple and accurate simulation method for multiparticle dynamics in an isodensity two-phase fluid system. The two-phase LBM is categorized into three models: the color-gradient model [11,12], the pseudopotential model [13,14], and the free-energy model [15,16]. Because the iSP method and free-energy model are based on the diffuse-interface model for representing two-phase solid-fluid and fluid-fluid systems, respectively, they should be compatible with each other. Among the several types of free-energy LBMs for two-phase fluids [15,16,25–27], the model developed by Inamuro *et al.* [28] was employed in this study.

Herein, we present a technique combining the iSP method and the free-energy model for the LBM simulation of wettable particles trapped at an interface between two immiscible isodensity fluids under gravity. The proposed technique was applied to five benchmark problems in two-dimensional systems: A, a stationary drop; B and C, a wettable particle trapped at a fluid-fluid interface in the absence or presence of gravity; D, two freely moving particles at a fluid-fluid interface in the presence of gravity; and E, two vertically constrained particles at a fluid-fluid interface. The results of these simulations were compared with theoretical estimations.

II. NUMERICAL MODELING

We consider a system in which N_p rigid particles with circular shapes are suspended in an incompressible Newtonian fluid consisting of two immiscible isodensity phases A and B. As shown in Fig. 1, two order parameters ϕ and ψ are employed, where ϕ distinguishes between the particle-side domain ($\phi = 1$) and fluid-side domain ($\phi = 0$), and the compositional order parameter ψ represents not only the fluids of phases A ($\psi = \psi_A$) and B ($\psi = \psi_B$), but also the fluid-wettable particles ($\psi = \psi_P$).

A. Improved smoothed profile (iSP) method

The SP method [29,30] assumes that the internal and interface domains of solid particles are filled with an artificial fluid with the same physical properties (i.e., density and viscosity)

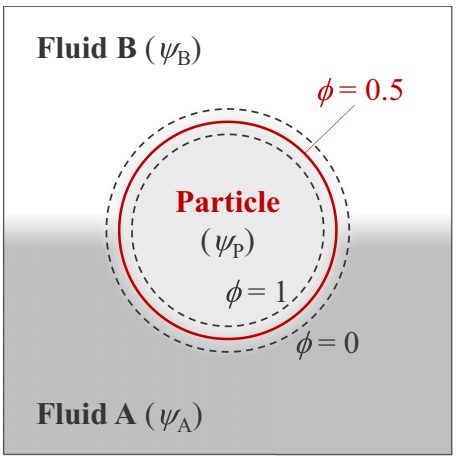

FIG. 1. Schematic illustration of a circular rigid particle suspended in an incompressible Newtonian fluid composed of two immiscible isodensity phases A and B. The order parameter ϕ distinguishes between the particle-side domain ($\phi = 1$) and fluid-side domain ($\phi = 0$), while the compositional order parameter ψ represents not only the fluid of phases A ($\psi = \psi_A$) and B ($\psi = \psi_B$) but also the fluid-wettable particle ($\psi = \psi_P$).

as the host fluid. The motion of this fluid flow is governed by the continuity equation and the modified momentum equation as follows:

$$\nabla \cdot \boldsymbol{u} = 0, \tag{1}$$

$$\frac{\partial \boldsymbol{u}}{\partial t} + (\boldsymbol{u} \cdot \nabla)\boldsymbol{u} = -\frac{1}{\rho_f}\nabla p + \nu_f \nabla^2 \boldsymbol{u} + \phi \boldsymbol{f}_p, \tag{2}$$

where $\boldsymbol{u}$ is the flow velocity of the fluid, p is its pressure, ρ_f is its mass density, and ν_f is its kinematic viscosity. The term $\phi \boldsymbol{f}_p$ represents the body force that enforces the no-slip conditions on rigid particle surfaces.

The translational and rotational motions of the kth particle ($k = 1, 2, \ldots, N_p$) with a circular shape are expressed by the following Newton-Euler equations:

$$\frac{d\boldsymbol{X}_k}{dt} = \boldsymbol{V}_k, \tag{3}$$

$$M_k \frac{d\boldsymbol{V}_k}{dt} = \boldsymbol{F}_k^H + \boldsymbol{F}_k^P + \boldsymbol{F}_k^G, \tag{4}$$

$$\boldsymbol{I}_k \cdot \frac{d\boldsymbol{\Omega}_k}{dt} = \boldsymbol{N}_k^H, \tag{5}$$

where $\boldsymbol{X}_k$, $\boldsymbol{V}_k$, $\boldsymbol{\Omega}_k$, M_k, and $\boldsymbol{I}_k$ are the center-of-mass position, translational velocity, angular velocity, mass, and inertial tensor of the kth particle, respectively. The terms $\boldsymbol{F}_k^H$ and $\boldsymbol{N}_k^H$ are the hydrodynamic force and torque, respectively, which are formulated in Sec. II B. The term $\boldsymbol{F}_k^P$ is the force arising from the excluded volume of particles that prevents the particles from overlapping with each other. In this study, $\boldsymbol{F}_k^P$ is neglected because particle contact never occurs. The term $\boldsymbol{F}_k^G$ represents a set of gravitational and buoyant forces as $\boldsymbol{F}_k^G = M_k(1 - \rho_f/\rho_p)\boldsymbol{a}_g$, where ρ_p is the mass density of the particles and $\boldsymbol{a}_g$ is the gravitational acceleration.

The original sharp interfaces between solid particles and a host fluid are replaced by diffuse interfaces with a finite thickness of ξ, as shown in Fig. 1. The existence of particles is expressed as a continuous field over the computational domain:

$$\phi(\boldsymbol{x}, t) = \sum_{k=1}^{N_p} \phi_k(\boldsymbol{x}, t), \tag{6}$$

where $\phi_k(\boldsymbol{x}, t)$ is the SP function for the kth particle at a fixed Eulerian lattice node $\boldsymbol{x}$ and time t. It is defined such that its profile continuously changes from $\phi_k = 1$ (particle-side domain) to $\phi_k = 0$ (fluid-side domain) within the interfacial domain (Fig. 1). In this paper, ϕ_k is defined as

$$\phi_k(\boldsymbol{x}) = s(R_k - |\boldsymbol{x} - \boldsymbol{X}_k|),$$
$$s(x) = \begin{cases} 0, & x < -\xi/2, \\ \frac{1}{2}\left[\sin\left(\frac{\pi x}{\xi}\right) + 1\right], & |x| \leqslant \xi/2, \\ 1, & x > \xi/2, \end{cases} \tag{7}$$

where R_k is the radius of the kth particle.

The particle velocity field $\boldsymbol{u}_p(\boldsymbol{x}, t)$ is defined using $\boldsymbol{X}_k$, $\boldsymbol{V}_k$, $\boldsymbol{\Omega}_k$, and ϕ_k as

$$\phi(\boldsymbol{x}, t)\boldsymbol{u}_p(\boldsymbol{x}, t) = \sum_{k=1}^{N_p} \phi_k(\boldsymbol{x}, t)[\boldsymbol{V}_k(t) + \boldsymbol{\Omega}_k(t) \times \{\boldsymbol{x} - \boldsymbol{X}_k(t)\}]. \tag{8}$$

The total (fluid + particle) velocity field $\boldsymbol{u}(\boldsymbol{x}, t)$ is then expressed as

$$\boldsymbol{u}(\boldsymbol{x}, t) = (1 - \phi)\boldsymbol{u}_f + \phi \boldsymbol{u}_p = \boldsymbol{u}_f + \phi(\boldsymbol{u}_p - \boldsymbol{u}_f). \tag{9}$$

To derive the evolution of the total velocity field $\boldsymbol{u}$, we solve for the fluid velocity $\boldsymbol{u}_f$. By integrating Eq. (2) without the body force term $\phi \boldsymbol{f}_p$, the total velocity is predicted as $\boldsymbol{u} = \boldsymbol{u}^*$ with a pressure that satisfies the incompressibility condition $\nabla \cdot \boldsymbol{u}^* = 0$. To enforce Eq. (9) and the solid-fluid impermeability condition, the time-integrated body force $\phi \boldsymbol{f}_p$ is calculated as

$$\int_t^{t+\Delta t} \phi \boldsymbol{f}_p dt' = \phi(\boldsymbol{x}, t + \Delta t)[\boldsymbol{u}_p(\boldsymbol{x}, t + \Delta t) - \boldsymbol{u}^*(\boldsymbol{x}, t + \Delta t)] - \frac{\Delta t}{\rho_f}\nabla p_p, \tag{10}$$

where the pressure p_p must satisfy $\nabla \cdot \boldsymbol{u} = (\nabla\phi) \cdot (\boldsymbol{u}_p - \boldsymbol{u}^*) = 0$. By correcting $\boldsymbol{u}^*$ using the body force, the total velocity field $\boldsymbol{u}(\boldsymbol{x}, t + \Delta t)$ is obtained. In this method, these calculations are conducted within the LBM framework, as described in Sec. II D.

In the iSP method [24], the effect of particle gravity ($\boldsymbol{F}_k^G$) on the motion of the isodensity fluid flow is implicitly considered in Eq. (2) via the term $\phi \boldsymbol{f}_p$, which is given by Eq. (10) with Eqs. (6)–(9). The hydrodynamic force $\boldsymbol{F}_k^H$ and torque $\boldsymbol{N}_k^H$ acting on the kth particle at a time t are calculated based on the momentum exchange between the particle and host fluid during the time interval Δt as follows:

$$\boldsymbol{F}_k^H(t) = \boldsymbol{F}_k^{H,tot}(t) + \boldsymbol{F}_k^{H,in}(t), \tag{11}$$

$$\boldsymbol{N}_k^H(t) = \boldsymbol{N}_k^{H,tot}(t) + \boldsymbol{N}_k^{H,in}(t), \tag{12}$$

where $\boldsymbol{F}_k^{H,tot}$ and $\boldsymbol{N}_k^{H,tot}$ are the hydrodynamic force and torque calculated using the original SP method [29,30], respectively, and $\boldsymbol{F}_k^{H,in}$ and $\boldsymbol{N}_k^{H,in}$ are the force and torque that compel the

velocity of the artificial fluid inside the kth particle to be consistent with the translational and rotational velocities of the particle, respectively. By considering the effect of internal fluid mass, the iSP method can calculate hydrodynamic force and torque more precisely, resulting in the stable and accurate computation of particle motion in various scenarios (see Ref. [24] for additional details).

B. Free-energy lattice Boltzmann method

In this study, a free-energy LBM with the two-dimensional nine-velocity (D2Q9) model [28,31] was adopted, where the physical space of interest is divided into a square lattice, and a fluid flow is represented by a collection of imaginary fluid particles with a finite set of velocity vectors. The nondimensional variables used hereafter are defined based on the characteristic quantities of length L_0, flow speed U_0, imaginary-particle speed c, time scale t_0 $(=L_0/U_0)$, and reference mass density ρ_0.

Let us consider an isodensity immiscible two-phase fluid, where fluid A coexists with fluid B (consider Fig. 1 without the particle). These two phases are distinguished by the compositional order parameter ψ, which is a function of position $\boldsymbol{x}$ in the spatial lattice. Fluids A and B are defined by the regions of $\psi(\boldsymbol{x}) = \psi_{\mathrm{A}}$ and $\psi(\boldsymbol{x}) = \psi_{\mathrm{B}}$ $(\psi_{\mathrm{A}} > \psi_{\mathrm{B}})$, respectively, and the region of intermediate values of $\psi_{\mathrm{B}} < \psi(\boldsymbol{x}) < \psi_{\mathrm{A}}$ is considered to be the interface between the two phases. The free-energy functional for this system is defined as

$$F[\psi] = \int d\boldsymbol{x}\Big[f_0(\psi) + \frac{\kappa_f}{2}|\nabla\psi|^2\Big], \tag{13}$$

where the first and second terms in the integral represent the bulk free-energy density and interfacial tension between the two fluids, respectively. f_0 can be expressed as a van der Waals–type free-energy density [28,31]:

$$f_0(\psi) = \psi T \ln\left(\frac{\psi}{1-b\psi}\right) - a\psi^2, \tag{14}$$

where the parameters a and b define the critical temperature as $T_{\mathrm{c}} = 8a/27b$ and the temperature T must be limited as $T < T_{\mathrm{c}}$ to derive ψ_{A} and ψ_{B}. The volume fraction of fluid A at a position $\boldsymbol{x}$ is expressed as

$$\Phi_{\mathrm{A}}(\boldsymbol{x}) = \frac{\psi(\boldsymbol{x}) - \psi_{\mathrm{B}}}{\psi_{\mathrm{A}} - \psi_{\mathrm{B}}}. \tag{15}$$

The pressure of this fluid is defined as

$$p_0 = \psi\frac{\partial f_0}{\partial\psi} - f_0 = \frac{\psi T}{1-b\psi} - a\psi^2. \tag{16}$$

The free-energy LBM employs a set of particle distribution functions $f_i(\boldsymbol{x},t)$ and $g_i(\boldsymbol{x},t)$ with velocities $\boldsymbol{c}_i$ $[=(0,0)$, $(\pm1,0)$, $(0,\pm1)$, and $(\pm1,\pm1)$ for $i = 1, 2, \ldots, 9]$ at a position $\boldsymbol{x}$ and time t. These functions evolve as follows:

$$f_i(\boldsymbol{x}+\boldsymbol{c}_i\Delta x,\ t+\Delta t) = f_i(\boldsymbol{x},\ t) - \frac{1}{\tau_f}\big[f_i(\boldsymbol{x},\ t) - f_i^{\mathrm{eq}}(\boldsymbol{x},\ t)\big], \tag{17}$$

$$g_i(\boldsymbol{x}+\boldsymbol{c}_i\Delta x,\ t+\Delta t) = g_i(\boldsymbol{x},\ t) - \frac{1}{\tau_g}\big[g_i(\boldsymbol{x},\ t) - g_i^{\mathrm{eq}}(\boldsymbol{x},\ t)\big], \tag{18}$$

where f_i^{eq} and g_i^{eq} are the equilibrium distribution functions, τ_f and τ_g are the dimensionless single relaxation times, Δx is the spacing of the square lattice, and Δt is the time step during which the particles travel across the lattice spacing. Note that $\Delta t = \mathrm{Sh}\Delta x$, where Sh denotes the Strouhal number and is defined by $\mathrm{Sh} = L_0/(t_0 c) = U_0/c$. In the presence of an external body force $\boldsymbol{f}(\boldsymbol{x},t)$, $g_i(\boldsymbol{x},t)$ evolves in fractional steps [31]. The intermediate value of g_i without a body force, denoted g_i^*, is calculated as

$$g_i^*(\boldsymbol{x}+\boldsymbol{c}_i\Delta x, t+\Delta t) = g_i(\boldsymbol{x},t) - \frac{1}{\tau_g}\big[g_i(\boldsymbol{x},t) - g_i^{\mathrm{eq}}(\boldsymbol{x},t)\big]. \tag{19}$$

Then, g_i can be obtained by correcting g_i^* using the body force as

$$g_i(\boldsymbol{x}, t+\Delta t) = g_i^*(\boldsymbol{x}, t+\Delta t) + 3\Delta x E_i \boldsymbol{c}_i \cdot \boldsymbol{f}(\boldsymbol{x}, t+\Delta t). \tag{20}$$

The compositional order parameter ψ, pressure p, and flow velocity $\boldsymbol{u}$ are calculated as

$$\psi(\boldsymbol{x},\ t) = \sum_{i=1}^{9} f_i(\boldsymbol{x},\ t), \tag{21}$$

$$p(\boldsymbol{x},\ t) = \frac{1}{3}\sum_{i=1}^{9} g_i(\boldsymbol{x},\ t), \tag{22}$$

$$\boldsymbol{u}(\boldsymbol{x},\ t) = \sum_{i=1}^{9} \boldsymbol{c}_i g_i(\boldsymbol{x},\ t). \tag{23}$$

The two equilibrium distribution functions are defined as

$$f_i^{\mathrm{eq}} = H_i\psi + F_i(p_0 - \kappa_f\psi\nabla^2\psi) + 3E_i\psi c_{i\alpha}u_\alpha + E_i\kappa_f G_{\alpha\beta}c_{i\alpha}c_{i\beta}, \tag{24}$$

$$g_i^{\mathrm{eq}} = E_i\Big[3p + 3c_{i\alpha}u_\alpha - \tfrac{3}{2}u_\alpha u_\alpha + \tfrac{9}{2}c_{i\alpha}c_{i\beta}u_\alpha u_\beta\Big] + E_i\kappa_g G_{\alpha\beta}c_{i\alpha}c_{i\beta}, \tag{25}$$

with

$$\begin{aligned} &E_1 = 4/9, \quad E_{2-5} = 1/9, \quad E_{6-9} = 1/36,\\ &H_1 = 1, \quad H_{2-9} = 0,\\ &F_1 = -5/3, \quad F_{2-5} = 1/3, \quad F_{6-9} = 1/12, \end{aligned} \tag{26}$$

$$G_{\alpha\beta} = \frac{9}{2}\frac{\partial\psi}{\partial x_\alpha}\frac{\partial\psi}{\partial x_\beta} - \frac{3}{2}\frac{\partial\psi}{\partial x_\gamma}\frac{\partial\psi}{\partial x_\gamma}\delta_{\alpha\beta}, \tag{27}$$

where κ_f and κ_g are constant parameters determining the interface width and interfacial tension, respectively [28,31]. In the above equations, the subscripts α, β, and γ represent the Cartesian coordinates $(\alpha,\beta,\gamma = x,y)$, $\delta_{\alpha\beta}$ is the Kronecker delta, and the summation convention is applied to α, β, and γ. The derivatives in Eqs. (24) and (27) are calculated using finite-difference approximations:

$$\frac{\partial\psi}{\partial x_\alpha} \approx \frac{1}{6\Delta x}\sum_{i=2}^{9} c_{i\alpha}\psi(\boldsymbol{x}+\boldsymbol{c}_i\Delta x), \tag{28}$$

$$\nabla^2\psi \approx \frac{1}{3(\Delta x)^2}\left[\sum_{i=2}^{9}\psi(\boldsymbol{x}+\boldsymbol{c}_i\Delta x) - 8\psi(\mathbf{x})\right]. \tag{29}$$

The transport coefficient M_f, kinematic viscosity ν_f, and interfacial tension σ are expressed as

$$M_\mathrm{f} = \frac{1}{3}\left(\tau_f - \frac{1}{2}\right)\Delta x, \tag{30}$$

$$\nu_\mathrm{f} = \frac{1}{3}\left(\tau_g - \frac{1}{2}\right)\Delta x, \tag{31}$$

$$\sigma = \kappa_g \int_{-\infty}^{\infty} \left(\frac{\partial \psi}{\partial \xi}\right)^2 d\xi, \tag{32}$$

respectively, where ξ is the coordinate normal to the interface.

C. Coupling between iSP method and free-energy LBM

The wettability of a solid particle surface in an immiscible two-phase fluid is represented according to Ref. [32], where the free-energy functional of Eq. (13) is replaced by

$$F[\psi, \phi] = \int d\boldsymbol{x}\left[f_0(\psi) + \frac{\kappa_f}{2}|\nabla\psi|^2 + \frac{\kappa_\mathrm{p}}{2}(\psi - \psi_\mathrm{p})^2\phi\right], \tag{33}$$

where the additional third term in the integral contains the particle field function $\phi(\boldsymbol{x}, t)$ of Eq. (6), as well as the compositional order parameter for the immiscible two-phase fluid, $\psi(\boldsymbol{x}, t)$ of Eq. (21), to represent the fluid-wettable surfaces of particles. ψ_p is a constant parameter for controlling wettability and κ_p is a positive parameter for constraining the compositional order parameter inside the particles to ψ_p. κ_p must be sufficiently large such that the free-energy density inside the particles without an interface, $f_0(\psi) + \kappa_\mathrm{p}(\psi - \psi_\mathrm{p})^2/2$, can exhibit a single-well profile with a minimum at $\psi \approx \psi_p$. In the presence of particles, p_0 in Eq. (24) must be replaced by

$$p_{0,\mathrm{p}} = \psi\frac{\partial f_{0,\mathrm{p}}}{\partial \psi} - f_{0,\mathrm{p}} = p_0 + \frac{\kappa_\mathrm{p}}{2}\left(\psi^2 - {\psi_\mathrm{p}}^2\right)\phi, \tag{34}$$

where

$$f_{0,\mathrm{p}}(\psi, \phi) = f_0(\psi) + \frac{\kappa_\mathrm{p}}{2}(\psi - \psi_\mathrm{p})^2\phi. \tag{35}$$

When the above modification is introduced, the order parameter exhibits a value of $\psi \approx \psi_\mathrm{p}$ within the particle domain and seamlessly changes to the original value of ψ for the host fluid outside the particle domain (Fig. 1). Consequently, the motion of contact points, where three phases of the solid particles and fluids A and B meet in the two-dimensional system, is represented thermodynamically.

D. Computational procedure

At the initial step ($t = 0$), $\boldsymbol{X}_k(0)$, $\boldsymbol{V}_k(0)$, $\boldsymbol{\Omega}_k(0)$, $\psi(\boldsymbol{x}, 0)$, $p(\boldsymbol{x}, 0)$, and $\boldsymbol{u}(\boldsymbol{x}, 0)$ are assigned, and $f_i(\boldsymbol{x}, 0)$ and $g_i(\boldsymbol{x}, 0)$ are assumed to be f_i^eq and g_i^eq, respectively, with $\psi(\boldsymbol{x}, 0)$, $p(\boldsymbol{x}, 0)$, and $\boldsymbol{u}(\boldsymbol{x}, 0)$, while $\boldsymbol{F}_k^\mathrm{H}(0)$ and $\boldsymbol{N}_k^\mathrm{H}(0)$ are assumed to be zero. It is also assumed that $\boldsymbol{X}_k(t)$, $\boldsymbol{V}_k(t)$, $\boldsymbol{\Omega}_k(t)$, $f_i(\boldsymbol{x}, t)$, $g_i(\boldsymbol{x}, t)$, $\psi(\boldsymbol{x}, t)$, $p(\boldsymbol{x}, t)$, and $\boldsymbol{u}(\boldsymbol{x}, t)$ are known immediately prior to their updating at time $t + \Delta t$. The computational procedure is presented below.

Step 1. Using the forces and torques at time t, $\boldsymbol{V}_k(t + \Delta t)$ and $\boldsymbol{\Omega}_k(t + \Delta t)$ are calculated using Eqs. (4) and (5) with the first-order explicit Euler scheme as follows:

$$\boldsymbol{V}_k(t + \Delta t) = \boldsymbol{V}_k(t) + \frac{\Delta t}{\mathrm{Sh}}{M_k}^{-1}\left[\boldsymbol{F}_k^\mathrm{H}(t) + \boldsymbol{F}_k^\mathrm{P}(t) + \boldsymbol{F}_k^\mathrm{G}(t)\right], \tag{36}$$

$$\boldsymbol{\Omega}_k(t + \Delta t) = \boldsymbol{\Omega}_k(t) + \frac{\Delta t}{\mathrm{Sh}}{\boldsymbol{I}_k}^{-1} \cdot \boldsymbol{N}_k^\mathrm{H}(t). \tag{37}$$

$\boldsymbol{X}_k(t + \Delta t)$ is then updated using Eq. (3) with the Crank-Nicolson scheme as follows:

$$\boldsymbol{X}_k(t + \Delta t) = \boldsymbol{X}_k(t) + \frac{\Delta t}{2\mathrm{Sh}}[\boldsymbol{V}_k(t) + \boldsymbol{V}_k(t + \Delta t)]. \tag{38}$$

Step 2. $\phi(\boldsymbol{x}, t + \Delta t)$ and $\boldsymbol{u}_\mathrm{p}(\boldsymbol{x}, t + \Delta t)$ are calculated using Eqs. (6)–(8) with $\boldsymbol{X}_k(t + \Delta t)$, $\boldsymbol{V}_k(t + \Delta t)$, and $\boldsymbol{\Omega}_k(t + \Delta t)$.

Step 3. $f_i(\boldsymbol{x}, t + \Delta t)$ is calculated using Eqs. (17) and (24) with $p_{0,\mathrm{p}}$ calculated using Eq. (34), and then $\psi(\boldsymbol{x}, t + \Delta t)$ is calculated using Eq. (21).

Step 4a. $g_i^*(\boldsymbol{x}, t + \Delta t)$ is calculated using Eqs. (19) and (25), and then $\boldsymbol{u}^*(\boldsymbol{x}, t + \Delta t)$ is calculated using Eq. (23) as follows:

$$\boldsymbol{u}^*(\boldsymbol{x}, t + \Delta t) = \sum_{i=1}^{9} \boldsymbol{c}_i g_i^*(\boldsymbol{x}, t + \Delta t). \tag{39}$$

The body force $\phi\boldsymbol{f}_\mathrm{p}$ is calculated using Eq. (10) as follows:

$$\phi\boldsymbol{f}_\mathrm{p}(\boldsymbol{x}, t + \Delta t) = \phi(\boldsymbol{x}, t + \Delta t)\frac{\mathrm{Sh}}{\Delta t}[\boldsymbol{u}_\mathrm{p}(\boldsymbol{x}, t + \Delta t) - \boldsymbol{u}^*(\boldsymbol{x}, t + \Delta t)]. \tag{40}$$

Step 4b. $g_i(\boldsymbol{x}, t + \Delta t)$ is calculated using Eq. (20) as follows:

$$g_i(\boldsymbol{x}, t + \Delta t) = g_i^*(\boldsymbol{x}, t + \Delta t) + 3\Delta x E_i \boldsymbol{c}_i \cdot \phi\boldsymbol{f}_\mathrm{p}(\boldsymbol{x}, t + \Delta t). \tag{41}$$

Then, $p(\boldsymbol{x}, t + \Delta t)$ and $\boldsymbol{u}(\boldsymbol{x}, t + \Delta t)$ are calculated using Eqs. (22) and (23), respectively.

Step 5. $\boldsymbol{F}_k^{\mathrm{H,tot}}(t + \Delta t)$ and $N_k^{\mathrm{H,tot}}(t + \Delta t)$ are calculated using Eq. (40) as follows:

$$\boldsymbol{F}_k^{\mathrm{H,tot}}(t + \Delta t) = -\frac{\mathrm{Sh}}{\Delta t}\rho_\mathrm{f}\sum_{\boldsymbol{x}\in\Omega^\mathrm{all}} \phi_k(\boldsymbol{x}, t + \Delta t) \times \boldsymbol{f}_\mathrm{p}(\boldsymbol{x}, t + \Delta t)(\Delta x)^2, \tag{42}$$

$$\boldsymbol{N}_k^{\mathrm{H,tot}}(t + \Delta t) = -\frac{\mathrm{Sh}}{\Delta t}\rho_\mathrm{f}\sum_{\boldsymbol{x}\in\Omega^\mathrm{all}} \phi_k(\boldsymbol{x}, t + \Delta t)[\boldsymbol{x} - \boldsymbol{X}_k(t + \Delta t)] \times \boldsymbol{f}_\mathrm{p}(\boldsymbol{x}, t + \Delta t)(\Delta x)^2, \tag{43}$$

where Ω^all is the entire domain of the system. $\boldsymbol{F}_k^{\mathrm{H,in}}$ and $\boldsymbol{N}_k^{\mathrm{H,in}}$ are calculated as

$$\boldsymbol{F}_k^{\mathrm{H,in}}(t + \Delta t) = \frac{\mathrm{Sh}}{\Delta t}\frac{\rho_\mathrm{f}}{\rho_\mathrm{p}}M_k[\boldsymbol{V}_k(t + \Delta t) - \boldsymbol{V}_k(t)], \tag{44}$$

$$\boldsymbol{N}_k^{\mathrm{H,in}}(t + \Delta t) = \frac{\mathrm{Sh}}{\Delta t}\frac{\rho_\mathrm{f}}{\rho_\mathrm{p}}\boldsymbol{I}_k \cdot [\boldsymbol{\Omega}_k(t + \Delta t) - \boldsymbol{\Omega}_k(t)], \tag{45}$$

respectively. Finally, $\boldsymbol{F}_k^\mathrm{H}(t + \Delta t)$ and $\boldsymbol{N}_k^\mathrm{H}(t + \Delta t)$ are calculated using Eqs. (11) and (12), respectively.

TABLE I. Systems for the simulations in this study.

System	N_p	$\alpha_1 = \alpha_2(\chi)$	$\rho_{p,1}/\rho_f$	$\rho_{p,2}/\rho_f$	$R/\Delta x$	$2\delta/\Delta x$	$(L_x/\Delta x) \times (L_y/\Delta x)$	$g/10^{-7}$	Bo	Illustration
A	0						128 × 128[a]	0		
B	1	0°–180° (from 1 to –1)	1.0		16		128 × 128[b]	0	0	Fig. 3(a)
C.1	1	45° (0.518)	0.2–1.6		16		256 × 256[c]	6.0	[−0.411, 0.3082]	Fig. 4(a)
C.2	1	90° (0)	0.2–1.8		16		256 × 256[c]	6.0	[−0.411, 0.411]	Fig. 4(a)
C.3	1	135° (−0.518)	0.4–1.8		16		256 × 256[c]	6.0	[−0.3082, 0.411]	Fig. 4(a)
D.1	2	135° (−0.518)	1.5	1.5	16	36−128	256 × 256[c]	6.0	0.257	Fig. 5(a)
D.2	2	135° (−0.518)	0.5	0.5	16	36−128	256 × 256[c]	6.0	−0.257	Fig. 5(b)
D.3	2	135° (−0.518)	1.5	0.5	16	36−128	256 × 256[c]	6.0	±0.257	Fig. 5(c)
E.1	2	45° (0.518)	1.0	1.0	16	64	256 × 256[d]	0	0	Figs. 5(a), 5(b)
E.2	2	90° (0)	1.0	1.0	16	64	256 × 256[d]	0	0	Figs. 5(a), 5(b)
E.3	2	135° (−0.518)	1.0	1.0	16	64	256 × 256[d]	0	0	Figs. 5(a), 5(b)

[a]A circular drop of phase A with a radius of $R_d = (10–50)\Delta x$ was placed at the center of a simulation cell represented by the 128 × 128 lattice nodes at $\boldsymbol{x} = (k\Delta x, l\Delta x)$ for $k, l = 1, 2, \ldots, 128$ (i.e., $L_x = L_y = 128\Delta x$), and the other region was filled with a host fluid of phase B. The periodic boundary condition was applied in all directions at $x = \Delta x$ and L_x and $y = \Delta x$ and L_y.

[b]The region containing the fluid and single particle was represented by the 128 × 128 lattice nodes at $\boldsymbol{x} = (k\Delta x, l\Delta x)$ for $k, l = 1, 2, \ldots, 128$ (i.e., $L_x = L_y = 128\Delta x$). The lower and upper halves of the simulation cell outside the particle domain were filled with fluids of phases A and B, respectively. The lower substrate at $y = 0$ had an affinity of $\psi_A(\chi = 1)$, while the upper substrate at $y = L_y + \Delta x$ had an affinity of $\psi_B(\chi = -1)$. The halfway free-slip boundary condition [17] was imposed on the fluid-side nodes at $y = \Delta x$ and L_y next to the solid-side nodes. The periodic boundary condition was applied on the sides at $x = \Delta x$ and L_x. Note that because the periodic boundary condition does not require a special treatment for the fluid-fluid interface, which might perturb the interface motion, the simulation results can be strictly compared with the simple theoretical estimations.

[c]Same as footnote b, but the larger system with $L_x = L_y = 256\Delta x$ contained two particles.

[d]Same as footnote c, but the area fraction of fluid phase A was set to the range of 0.43–0.57.

III. RESULTS AND DISCUSSION

To test the performance of the proposed method, we considered five types of benchmark problems: A, a stationary drop; B and C, a wettable particle trapped at a fluid-fluid interface in the absence or presence of gravity; D, two freely moving particles at a fluid-fluid interface in the presence of gravity (i.e., capillary floatation forces [2,3]); and E, two vertically constrained particles at a fluid-fluid interface (i.e., capillary immersion forces [2,3]). The details of these five systems are summarized in Table I, where N_p is the number of particles, α is the contact angle of a particle against fluid A in fluid B, ρ_p and R are the mass density and the radius of the particles, respectively, g is the acceleration of gravity, and the subscripts 1 and 2 represent the left- and right-hand-side particles, respectively, in the case of $N_p = 2$. The size of simulation cell, $L_x \times L_y$, for every system was set such that (i) the periodic boundary conditions hardly affected the behaviors of a stationary drop for system A and (ii) the boundary conditions at the lower and upper walls barely influenced the behaviors of the particle(s) at the mechanically equilibrated state for systems B–E.

The following parameters were fixed for the simulations of every system, although it is easy to improve the calculation accuracy by tuning the parameters depending on the simulation system. The constant values of Δx and Δt were employed, giving the constant value of Strouhal number $\mathrm{Sh}(=\Delta t/\Delta x)$. A thickness of $\xi = 2\Delta x$ was used for the SP function of Eq. (7), whereby the hydrodynamic force acting on a particle with the radius of $R = 16\Delta x$ was reproduced with satisfactory accuracy [24]. The parameters determining the free-energy density of Eq. (14) were set to $a = 1$, $b = 1$, and $T = 0.293$, resulting in values of the compositional order parameters for the two fluid phases of $\psi_A = 0.403$ and $\psi_B = 0.264$. The relaxation times for f_i and g_i were $\tau_f = 1.0$ and $\tau_g = 0.65$, respectively, which were determined by consideration of the balance between computational time and stability after our preliminary simulations. Although the values of τ_f and τ_g determined the transport coefficient and kinematic viscosity of an immiscible two-phase fluid flow via Eqs. (30) and (31), respectively, they should never affect the present simulation results at the mechanically equilibrated state (except for Fig. 8). The parameters determining interfacial tension were $\kappa_f = 0.05(\Delta x)^2$ and $\kappa_g = 0.1(\Delta x)^2$, resulting in an interfacial tension of $\sigma = (2.99 \times 10^{-4})\Delta x$ according to Eq. (32) with the simulated profile of compositional order parameter for a flat fluid-fluid interface (see Sec. III A and the Appendix). The compositional order parameters inside the particle domain were approximately constrained to a value of ψ_p ranging from ψ_B to ψ_A by setting $\kappa_p = 0.2(\Delta x)^2$.

A. Single stationary liquid drop

Let us consider system A in Table I, where a circular drop of phase A with a radius of R_d in a host fluid of phase B was simulated. Figure 2 shows the pressure difference ΔP between a circular drop of phase A with a radius of R_d and the surrounding fluid of phase B as a function of ${R_d}^{-1}$. The simulation results quantitatively agree with the theoretical

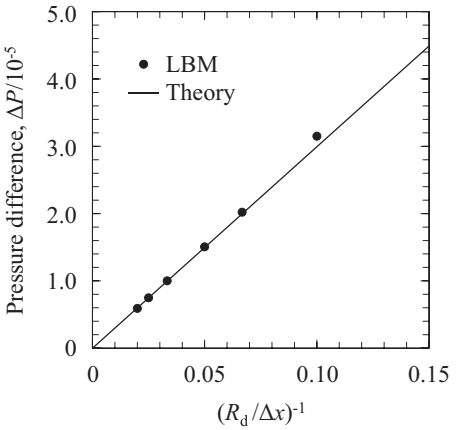

FIG. 2. Pressure difference ΔP between a circular drop of phase A with a radius of R_d and a host fluid of phase B as a function of $R_d{}^{-1}$ for system A (see Table I). The filled circles represent the simulation results, and the solid line represents the theoretical estimations based on Laplace's law [Eq. (46)] with an interfacial tension of $\sigma = (2.99 \times 10^{-4})\Delta x$.

estimation based on Laplace's law:

$$\Delta P^{\rm th} = \frac{\sigma}{R_{\rm d}}, \tag{46}$$

where the interfacial tension was calculated as $\sigma = (2.99 \times 10^{-4})\Delta x$, using Eq. (32) with the simulated profile of compositional order parameter (see the Appendix). The fluid-fluid interface had a width of $\sim 10\Delta x$, which was comparable to the radius of the smallest drop (i.e., $R_{\rm d} = 10\Delta x$). Fitting Eq. (32) to the simulation data for the sufficiently large drops (i.e., $R_{\rm d} \geqslant 15\Delta x$) resulted in $\sigma = (3.01 \times 10^{-4})\Delta x$. These results demonstrate that the proposed two-phase LBM solver with the parameters described above can accurately describe a fluid-fluid interface.

In computational fluid dynamics, one often encounters spurious currents, which are unphysical velocities appearing near a fluid-fluid interface due to force imbalance between the interfacial tension and pressure gradient; such spurious currents become more significant for the two-phase fluids with the larger density ratio [33]. The spurious currents were found to be negligibly small in the present simulations, where the isodensity two-phase fluid systems were considered.

B. Single particle trapped at flat fluid-fluid interface in absence of gravity

Let us consider system B in Table I to investigate the wettability of a particle surface for an immiscible two-phase fluid. A particle trapped at a fluid-fluid interface was simulated in the absence of gravity, as shown in Fig. 3(a). A circular particle with radius R, mass density $\rho_{\rm p}(=\rho_{\rm f})$, and wettability of χ was initially placed at the center of the simulation cell, and then allowed to move toward a mechanically equilibrated position. Here, χ denotes the affinity of the kth particle with $\bar{\psi}_{\rm p}$ for a fluid of phase A and is defined as [34]

$$\chi = \frac{\bar{\psi}_{\rm p} - \psi_0}{\psi_{\rm A} - \psi_0}, \tag{47a}$$

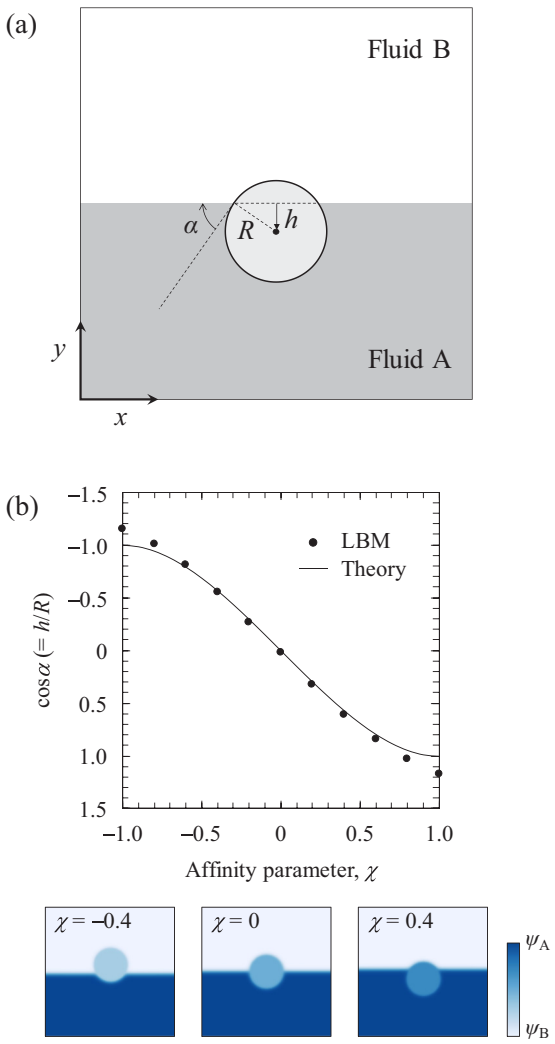

FIG. 3. (a) Schematic illustration of system B (see Table I) in a mechanically equilibrated state, where a circular particle with a radius of R, mass density of $\rho_{\rm p}$ $(=\rho_{\rm f})$, and contact angle of α $(< 90°)$ is trapped at a flat fluid-fluid interface in the absence of gravity, exhibiting a downward distance h from the fluid-fluid interface to the particle center. (b) The value of $\cos\alpha(=h/R)$ as a function of the affinity parameter χ defined by Eq. (47). The filled circles represent the simulation results, and the solid line represents the theoretical estimations based on Eq. (49).

$$\bar{\psi}_{\rm p} = \int d\boldsymbol{x}\ \psi(\boldsymbol{x})\phi_k(\boldsymbol{x}) \Big/ \int d\boldsymbol{x}\ \phi_k(\boldsymbol{x}) \approx \frac{1}{\pi R_k^2}\int d\boldsymbol{x}\ \psi(\boldsymbol{x})\phi_k(\boldsymbol{x}), \tag{47b}$$

$$\psi_0 = \frac{\psi_{\rm A} + \psi_{\rm B}}{2}. \tag{47c}$$

At the mechanically equilibrated state, the fluid-fluid interface capturing the wettable particle was not deformed but horizontally flat due to the absence of gravity. Throughout this study, the spatial location of fluid-fluid interface was defined as a series of positions giving $\psi(\boldsymbol{x}) = \psi_0$. The contact angle α of the particle was then calculated as

$$\cos\alpha = \frac{h}{R}, \tag{48}$$

where h is the downward distance from the fluid-fluid interface to the center of the particle. Figure 3(b) displays $\cos\alpha$ as a function of the affinity parameter χ, demonstrating that the simulation results agree well with the theoretical estimation [34]:

$$\cos\alpha^{\text{th}} = \frac{\sigma_{\text{pB}} - \sigma_{\text{pA}}}{\sigma} = \frac{\chi}{2}(3 - \chi^2), \tag{49}$$

where σ_{pA} (or σ_{pB}) denotes the interfacial tension between the particle surface and phase-A fluid (or phase-B fluid). Therefore, our model can successfully represent a wide range of wettability of particle surfaces by tuning the affinity parameter χ (for more details, see the Appendix).

C. Single particle trapped at deformed fluid-fluid interface in presence of gravity

Let us consider system C in Table I, where a wettable particle is trapped at a fluid-fluid interface in the presence of gravity, as illustrated in Fig. 4(a). This particle moves toward its mechanically equilibrated position.

1. Theoretical description of system C

In the mechanically equilibrated state, the fluid-fluid interface arresting a particle with a radius of R, mass density of ρ_{p}, and contact angle of α (i.e., wettability of χ) is deformed due to the downward gravitational field g. The slope angle of the fluid-fluid interface Ψ at the point of contact between the interface and particle surface, and the downward distance h from the interface to the center of the particle are determined by the Bond number:

$$\text{Bo} = \frac{R^2(\rho_{\text{p}} - \rho_{\text{f}})g}{\sigma}, \tag{50}$$

which represents a balance between the surface tension force and the gravitational force. The deformed fluid-fluid interface exhibits a circular arc shape with a curvature radius of R_{c} and a central angle of Ψ. The pressure difference ΔP between the lower- and upper-side fluids across the deformed interface is calculated using Laplace's law:

$$\Delta P = \frac{\sigma}{R_{\text{c}}}. \tag{51}$$

The resultant force from ΔP acts on the partially wetted particle having two points of contact with the fluid-fluid interface, and the direct distance between these two contact points is given by $2(L - R_{\text{c}}\sin\Psi)$, where $L = L_x/2$. The force balance in the vertical direction is then expressed as

$$2\sigma\sin\Psi + 2(L - R_{\text{c}}\sin\Psi)\Delta P - \pi R^2(\rho_{\text{p}} - \rho_{\text{f}})g = 0. \tag{52}$$

Although Fig. 4(a) corresponds to the case of a heavy-weight particle (i.e., $\rho_{\text{p}} > \rho_{\text{f}}$), Eqs. (50)–(52) remain applicable to the case of a light-weight particle (i.e., $\rho_{\text{p}} < \rho_{\text{f}}$), where Bo, Ψ, R_{c}, and ΔP have negative values. In the case of $\rho_{\text{p}} = \rho_{\text{f}}$, the fluid-fluid interface is not deformed but rather horizontally flat, as described in Sec. III B, where Bo, Ψ, and ΔP are zero.

In the case of $\rho_{\text{p}} \neq \rho_{\text{f}}$ (i.e., Bo $\neq 0$), Eq. (50) with Eqs. (51) and (52) yields

$$R_{\text{c}} = \frac{2L\sigma}{\pi R^2(\rho_{\text{p}} - \rho_{\text{f}})g} = \frac{2L}{\pi\text{Bo}}. \tag{53}$$

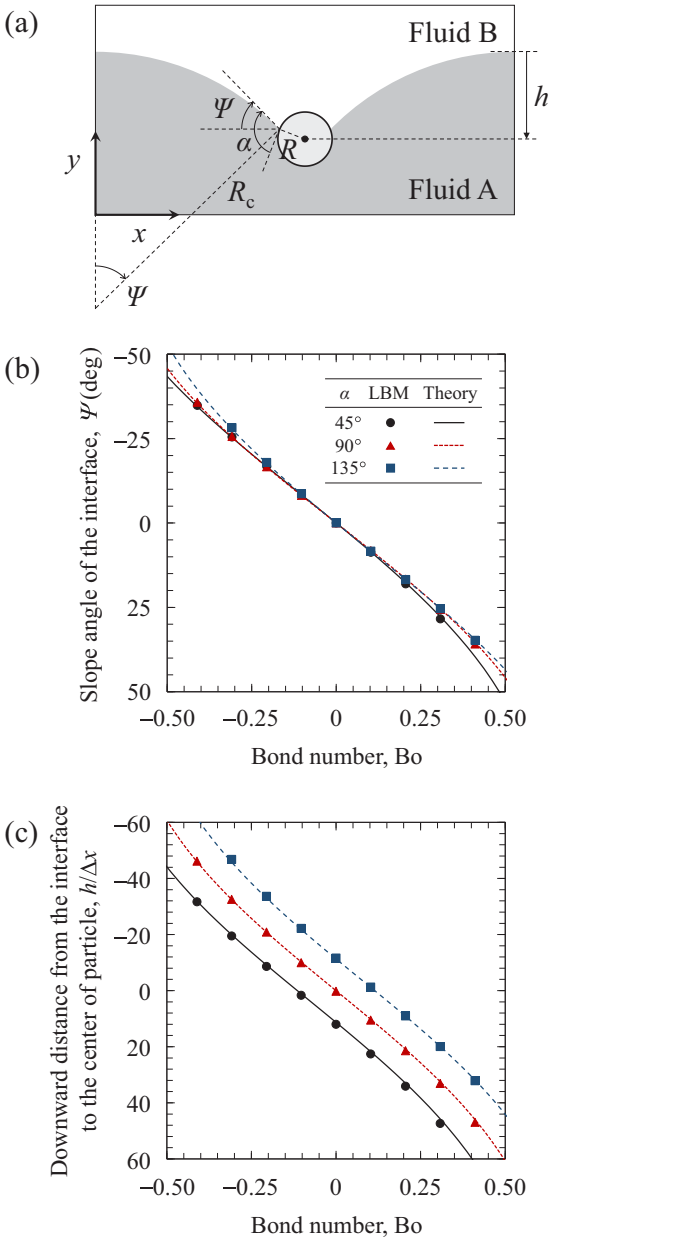

FIG. 4. (a) Schematic illustration of system C (see Table I) in a mechanically equilibrated state, where a circular particle with a radius of R, mass density of $\rho_{\text{p}}(>\rho_{\text{f}})$, and contact angle of $\alpha(>90^\circ)$ is trapped at a deformed fluid-fluid interface in the presence of gravity, exhibiting a downward distance h from the fluid-fluid interface to the particle center and a slope angle of the fluid-fluid interface Ψ at the point of contact between the interface and the particle surface. The deformed fluid-fluid interface exhibits a circular arc shape with a curvature radius of R_{c} and central angle of Ψ. (b), (c) Values of Ψ and h, respectively, as a function of the Bond number, Bo, defined by Eq. (50). The filled symbols represent the simulation results for the cases of $\alpha = 45^\circ$, 90°, and 135°, and the lines represent the theoretical estimations of Ψ from Eqs. (56) and (57) and those of h from Eq. (58).

Because the line segment between the contact point and the center of the particle trapped at the fluid-fluid interface has a slope angle of $\pi/2 - \alpha + \Psi$, the curvature radius of the

interface R_c satisfies

$$L = R\cos\left(\frac{\pi}{2} - \alpha + \Psi\right) + R_c \sin\Psi$$
$$= R\sin(\alpha - \Psi) + R_c \sin\Psi. \quad (54)$$

Equations (53) and (54) follow the quadratic equation for sin Ψ,

$$\left({R_c}^2 + R^2 - 2R_c R\cos\alpha\right)\sin^2\Psi - 2L(R_c - R\cos\alpha)\sin\Psi + L^2 - R^2\sin^2\alpha = 0. \quad (55)$$

The angle Ψ is calculated as

$$\Psi = \sin^{-1}\left[\frac{-B \pm \sqrt{B^2 - AC}}{A}\right] \quad \text{for Bo} \gtrless 0, \quad (56)$$

with

$$A = {R_c}^2 + R^2 - 2R_c R\cos\alpha,$$
$$B = -L(R_c - R\cos\alpha),$$
$$C = L^2 - R^2\sin^2\alpha. \quad (57)$$

The downward distance from the interface to the center of the particle, h, is expressed as

$$h = R\sin\left(\frac{\pi}{2} - \alpha + \Psi\right) + R_c(1 - \cos\Psi)$$
$$= R\cos(\alpha - \Psi) + R_c(1 - \cos\Psi). \quad (58)$$

The condition for system stability is given by considering the physically possible values of Ψ in Eq. (56) with Eq. (57):

$$-\frac{\frac{2L}{R}\left[\sqrt{\left(\frac{L}{R}\right)^2 - (\sin\alpha)^2} + \cos\alpha\right]}{\left(\frac{L}{R}\right)^2 - 1}$$
$$\leqslant \pi\,\text{Bo} \leqslant \frac{\frac{2L}{R}\left[\sqrt{\left(\frac{L}{R}\right)^2 - (\sin\alpha)^2} - \cos\alpha\right]}{\left(\frac{L}{R}\right)^2 - 1}, \quad (59)$$

where $L > R$. Once the values of L, R, and α are given, the range of physically possible values of Bo is obtained using Eq. (59).

Similar systems were investigated by Onishi *et al.* [19], where the contact angle of the particle was restricted to $\alpha = 90^\circ$ in Eqs. (54)–(59) and the second term of Eq. (52) for the pressure difference between the lower- and upper-side fluids across the deformed interface was neglected.

2. Simulations of system C

Several different values of Bo were selected by varying the mass density of a particle ρ_p to satisfy the stability condition of Eq. (59), where both light- and heavy-weight particles were simulated (Table I). A circular particle with a radius of R, mass density of $\rho_p (\neq \rho_f)$, and contact angle of α (i.e., wettability of χ) was initially placed at the center of the simulation cell and then allowed to move toward its mechanically equilibrated position in the gravitational field. When the particle was located in the mechanically equilibrated position, the tangential slope of the deformed fluid-fluid interface at the contact point, tan Ψ, and the downward distance from the interface to the particle center, h, were measured. Figures 4(b) and 4(c) present the results of the present simulations in comparison with the theoretical estimations from Eqs. (56) and (57) and Eq. (58), respectively. The simulation results and theoretical estimations agree well with each other for every contact angle of the particle, regardless of particle weight (i.e., Bo > 0 and Bo < 0). It should be noted that the accurate and stable computation of the motion of light-weight particles is one of the advantages of the iSP method [24].

D. Capillary floatation force: Two freely moving particles at fluid-fluid interface in presence of gravity

Let us consider system D in Table I, where two wettable particles trapped at a fluid-fluid interface are freely moving in the presence of gravity, as shown in Fig. 5: (a) two heavy-weight particles, (b) two light-weight particles, and (c) one heavy-weight particle and one light-weight particle. The two freely moving particles under gravity experience a capillary floatation force in the horizontal direction.

Similar systems were investigated in previous studies [19–21,35], where the motions of particles were evaluated qualitatively. Onishi *et al.* [19] compared simulation results with theoretical results, where the mass density and contact angle of the particles were restricted to $\rho_p > \rho_f$ and $\alpha = 90^\circ$, respectively. In this study, the capillary flotation force between two particles with arbitrary values of ρ_p and α was theoretically formulated, and comparisons between the simulation and theoretical results are presented.

1. Theoretical description of system D

a. Two identical particles. Figure 5(a) [or 5(b)] illustrates a system containing two identical heavy-weight (or light-weight) particles with a mass density of $\rho_p > \rho_f$ (or $\rho_p < \rho_f$), radius of R, and contact angle of α (i.e., wettability of χ) trapped at a fluid-fluid interface, where the horizontal center-to-center distance between the particles is denoted as 2δ and the downward distance from the interface to each particle center is represented by h. The slope angle of the wide-gap fluid-fluid interface at the point of contact between the interface and the particle surface is represented by Ψ, while that of the narrow-gap fluid-fluid interface is denoted as Ψ'. At the mechanically equilibrated state, the wide-gap and narrow-gap interfaces exhibit circular arc shapes of the same curvature radius of R_c with central angles of Ψ and Ψ', respectively. It should be noted that the signs of Ψ, Ψ', and R_c as well as ΔP, Bo, and h for heavy-weight particles ($\rho_p > \rho_f$) are positive, whereas those for light-weight particles ($\rho_p < \rho_f$) are negative.

The force balance equations in the horizontal and vertical directions are given as follows:

$$F^{\text{lat}} = \sigma(\cos\Psi - \cos\Psi') + R\left\{-\sin\left(\frac{\pi}{2} - \alpha + \Psi\right) + \sin\left(\frac{\pi}{2} - \alpha + \Psi'\right)\right\}\Delta P, \quad (60)$$

$$\sigma(\sin\Psi + \sin\Psi') + R\left\{\cos\left(\frac{\pi}{2} - \alpha + \Psi\right) + \cos\left(\frac{\pi}{2} - \alpha + \Psi'\right)\right\}\Delta P - \pi R^2(\rho_p - \rho_f)g = 0, \quad (61)$$

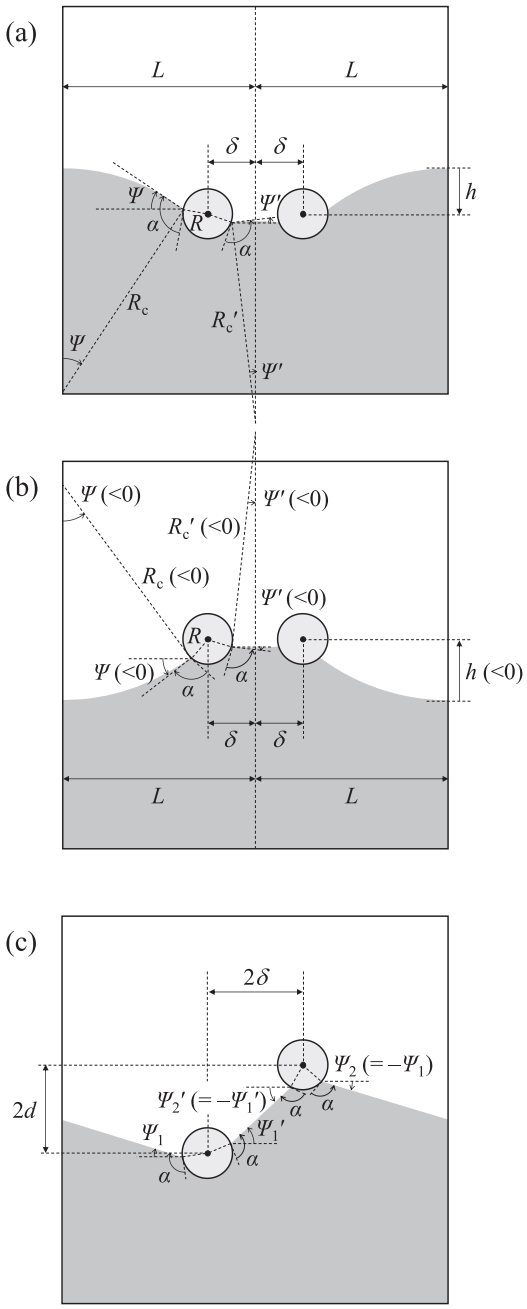

FIG. 5. Schematic illustrations of system D (see Table I) in a mechanically equilibrated state, where two freely moving particles with the same radius R and contact angle α ($> 90^\circ$) are transiently separated by a horizontal center-to-center distance of 2δ and trapped at a deformed fluid-fluid interface in the presence of gravity, experiencing a capillary floatation force in the horizontal direction: (a) two identical heavy-weight particles with a mass density of $\rho_p > \rho_f$, (b) two identical light-weight particles with $\rho_p < \rho_f$, and (c) two similar particles with different mass densities ($\rho_{p,1} = \rho_f + \Delta\rho$ and $\rho_{p,2} = \rho_f - \Delta\rho$). The other mathematical symbols are explained in the main text.

where $F^{\rm lat} > 0$ and $F^{\rm lat} < 0$ represent repulsive and attractive forces between two particles in the horizontal direction, respectively. The pressure difference ΔP in Eqs. (60) and (61) is given by Eq. (51) with a different expression of R_c from Eq. (53). The curvature radius of R_c in Fig. 5(a) must satisfy

$$L - \delta = R\cos\left(\frac{\pi}{2} - \alpha + \Psi\right) + R_c \sin\Psi, \tag{62}$$

$$\delta = R\cos\left(\frac{\pi}{2} - \alpha + \Psi'\right) + R_c \sin\Psi'. \tag{63}$$

Equation (61) with Eqs. (62), (63), and (51) yields

$$R_c = \frac{L\sigma}{\pi R^2(\rho_p - \rho_f)g} = \frac{L}{\pi \mathrm{Bo}}. \tag{64}$$

Equations (62) and (63) with Eq. (64) yield the following quadratic equations for $\sin\Psi$ and $\sin\Psi'$:

$$\left({R_c}^2 + R^2 - 2R_c R\cos\alpha\right)\sin^2\Psi - 2(L-\delta)(R_c - R\cos\alpha) \times \sin\Psi + (L-\delta)^2 - R^2\sin^2\alpha = 0, \tag{65}$$

$$\left({R_c}^2 + R^2 - 2R_c R\cos\alpha\right)\sin^2\Psi' - 2\delta(R_c - R\cos\alpha)\sin\Psi' + \delta^2 - R^2\sin^2\alpha = 0, \tag{66}$$

respectively. The angles Ψ and Ψ' are calculated using Eq. (56) with

$$A = {R_c}^2 + R^2 - 2R_c R\cos\alpha,$$
$$B = -(L-\delta)(R_c - R\cos\alpha),$$
$$C = (L-\delta)^2 - R^2\sin^2\alpha, \tag{67}$$

and

$$A = {R_c}^2 + R^2 - 2R_c R\cos\alpha,$$
$$B = -\delta(R_c - R\cos\alpha),$$
$$C = \delta^2 - R^2\sin^2\alpha, \tag{68}$$

respectively, where Ψ in Eq. (56) should be replaced with Ψ' for the angle of Ψ'. The lateral force $F^{\rm lat}$ is then calculated using Eq. (60) with the obtained values of Ψ and Ψ', as well as the preset values of σ, R, α, and ΔP [i.e., Eq. (51) with Eqs. (64) and (50)]. The downward distance from the interface to the center of the particle, h, is calculated using Eq. (58). The condition for system stability is determined by considering the presence of physically possible values of Ψ and Ψ' in Eq. (56) with Eqs. (67) and (68):

$$-\frac{\frac{L}{R}\left[\sqrt{\left(\frac{L-\delta}{R}\right)^2 - (\sin\alpha)^2} + \cos\alpha\right]}{\left(\frac{L-\delta}{R}\right)^2 - 1} \leqslant \pi\,\mathrm{Bo} \leqslant \frac{\frac{L}{R}\left[\sqrt{\left(\frac{L-\delta}{R}\right)^2 - (\sin\alpha)^2} - \cos\alpha\right]}{\left(\frac{L-\delta}{R}\right)^2 - 1}, \tag{69}$$

where $L/2 > \delta \geqslant R$. When the values of L, δ, R, and α are known, the range of physically possible values of Bo can be obtained using Eq. (69).

b. Two similar particles with different mass densities. Figure 5(c) illustrates a system containing two similar particles with the same radius R, same wettability χ, and different mass densities ($\rho_{p,1} = \rho_f + \Delta\rho$ and $\rho_{p,2} = \rho_f - \Delta\rho$) trapped at a fluid-fluid interface, where the horizontal center-to-center distance between the two particles is denoted as 2δ and the vertical distance between the two particles is denoted as $2d$.

The downward gravitational force on particle 1 is exactly equal in magnitude to the upward gravitational force on particle 2. At the mechanically equilibrated state, the wide- and narrow-gap fluid-fluid interfaces around these particles exhibit straight lines, but they are inclined rather than horizontal. Consequently, they have a curvature of $1/R_c = 0$ and the resultant pressure difference between the lower- and upper-side fluids, $\Delta P = 0$, according to Eq. (51), exhibiting slope angles of $\Psi_2 = -\Psi_1 < 0$ and $\Psi_2' = -\Psi_1' < 0$.

The force balance equations for particle 1 in the horizontal and vertical directions are respectively given as

$$F^{\rm lat} = \sigma(\cos\Psi_1 - \cos\Psi_1'), \tag{70}$$

$$\sigma(\sin\Psi_1 + \sin\Psi_1') - \pi R^2 g\Delta\rho = 0, \tag{71}$$

with equivalent equations for particle 2. From a geometrical perspective, the slope angles of Ψ_1 and Ψ_1' are respectively calculated as

$$\Psi_1 = \sin^{-1}\left[\frac{d}{\sqrt{(L-\delta)^2 + d^2}}\right], \tag{72}$$

$$\Psi_1' = \sin^{-1}\left[\frac{d}{\sqrt{\delta^2 + d^2}}\right]. \tag{73}$$

Equation (71) with Eqs. (72), (73), and (50) yield

$$\frac{d}{\sqrt{(L-\delta)^2 + d^2}} + \frac{d}{\sqrt{\delta^2 + d^2}} - \pi|{\rm Bo}| = 0. \tag{74}$$

The condition for system stability is determined by considering the presence of physically possible values of d in Eq. (74):

$$\pi|{\rm Bo}| < 2. \tag{75}$$

Once the values of the parameters are preset under the condition of Eq. (75), the value of d is obtained numerically using Eq. (74) and Ψ_1 and Ψ_1' are then calculated using Eqs. (72) and (73), respectively. Consequently, $F^{\rm lat}$ is calculated using Eq. (70). It should be noted that the wettability χ of two similar particles with different mass densities ($\rho_{{\rm p},1} = \rho_{\rm f} + \Delta\rho$ and $\rho_{{\rm p},2} = \rho_{\rm f} - \Delta\rho$) never influence the values of $F^{\rm lat}$, Ψ_1, Ψ_1', and d. This is not the case for two identical particles, as indicated by Eqs. (56), (58), and (60) with Eqs. (67) and (68).

2. *Simulations of system D*

As an initial condition of system D in Table I, two circular particles with mass densities of $\rho_{{\rm p},1}$ and $\rho_{{\rm p},2}$ ($\neq \rho_{\rm f}$) were separated by an interparticle distance of 2δ ($< L$) and placed at a flat fluid-fluid interface. The two particles were then allowed to move in the vertical direction under gravity toward their mechanically equilibrated positions. Figure 6 shows snapshots of system D at the mechanically equilibrated states for horizontal interparticle distances of $2\delta = 48\Delta x$ and $96\Delta x$ (i.e., $2\delta = 3R$ and $6R$). Regardless of particle weight combination and interparticle distance, the heavy-weight particle with $\rho_{\rm p} = 1.5\rho_{\rm f}$ resides below the level of the fluid-fluid interface away from a pair of the particles, whereas the light-weight particle with $\rho_{\rm p} = 0.5\rho_{\rm f}$ resides above the level. This behavior is determined by the balance between the values of Bo and α, as shown in Fig. 4(c).

In the cases of a pair of identical heavy-weight [Fig. 5(a)] or light-weight [Fig. 5(b)] particles, the downward distance

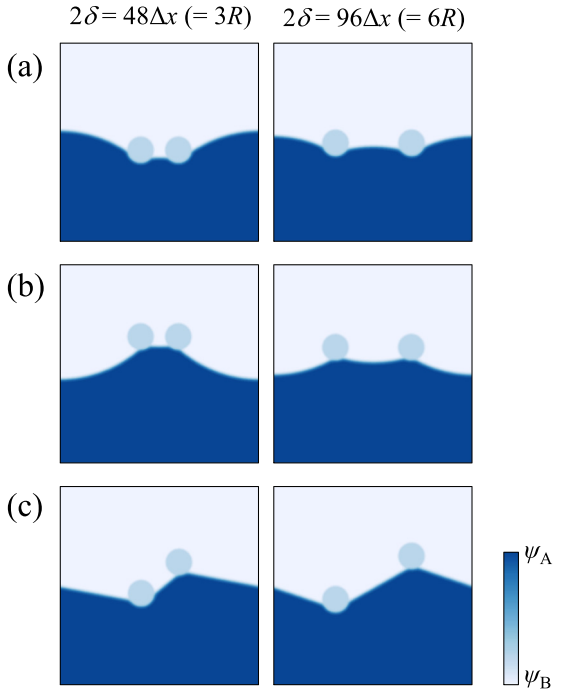

FIG. 6. Snapshots for the simulation of system D (see Fig. 5) in a mechanically equilibrated state: (a) Two identical heavy-weight particles with $\rho_{{\rm p},1} = \rho_{{\rm p},2} = 1.5\rho_{\rm f}$, (b) two identical light-weight particles with $\rho_{{\rm p},1} = \rho_{{\rm p},2} = 0.5\rho_{\rm f}$, and (c) two similar particles with different mass densities of $\rho_{{\rm p},1} = 1.5\rho_{\rm f}$ and $\rho_{{\rm p},2} = 0.5\rho_{\rm f}$, where a contact angle of $\alpha = 135^\circ$ was employed throughout system D (see Table I). The left- and right-hand sides of every panel display snapshots at horizontal interparticle distances of $2\delta = 48\Delta x\ (= 3R)$ and $2\delta = 96\Delta x\ (= 6R)$, respectively.

of the particle centers from the interface, h, increased in magnitude with a decrease in 2δ, as shown in Fig. 7(a). In contrast, the particle pair with $\rho_{{\rm p},1} = 1.5\rho_{\rm f}$ and $\rho_{{\rm p},2} = 0.5\rho_{\rm f}$ is a special case corresponding to Fig. 5(c), where the wide- and narrow-gap fluid-fluid interfaces between the two particles exhibited inclined straight lines, as shown in Fig. 6(c). Their vertical interparticle distance, $2d$, decreased with a decrease in 2δ, as shown in Fig. 7(a). The simulation results for h and $2d$ agreed closely with the theoretical estimations from Eqs. (58) and (74), respectively.

As shown in Fig. 6, the fluid-fluid interface around the particles became more distorted with a decrease in 2δ, which resulted in a stronger lateral force $F^{\rm lat}$, as shown in Fig. 7(b). Identical particle pairs with heavy weight or light weight experienced attractive forces, whereas repulsive forces acted between the heavy- and light-weight particles. This behavior is characteristic of a capillary floatation force. Figure 7(b) reveals that the simulation results agree with the theoretical estimations from Eqs. (60) and (70). The agreement regarding $F^{\rm lat}$ worsened with a decrease in 2δ, especially at distances of $2\delta < 40\Delta x\ (= 2.5R)$. This discrepancy was caused by overlap between two wetting layers of a two-phase fluid around wettable particles, and could be diminished by reducing the width of a diffuse fluid-fluid interface and/or using the larger particles. More detailed examinations as well as improvements of the proposed model will be our future work.

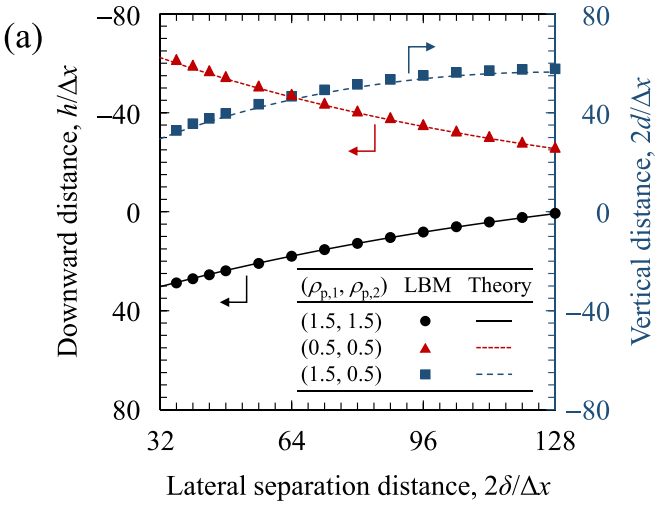

FIG. 7. Simulation results (filled symbols) and theoretical estimations (lines) for system D, corresponding to Figs. 5 and 6: (a) the downward distance h for two identical particles (left-hand-side axis) or the vertical distance $2d$ between two similar particles with different mass densities (right-hand-side axis) as a function of their center-to-center distance 2δ; (b) the capillary floatation force F^{lat} between the two particles in the horizontal direction as a function of 2δ. The lines in panels (a) and (b) represent the theoretical estimations from Eq. (58) or (74) and those from Eqs. (60) or (70), respectively.

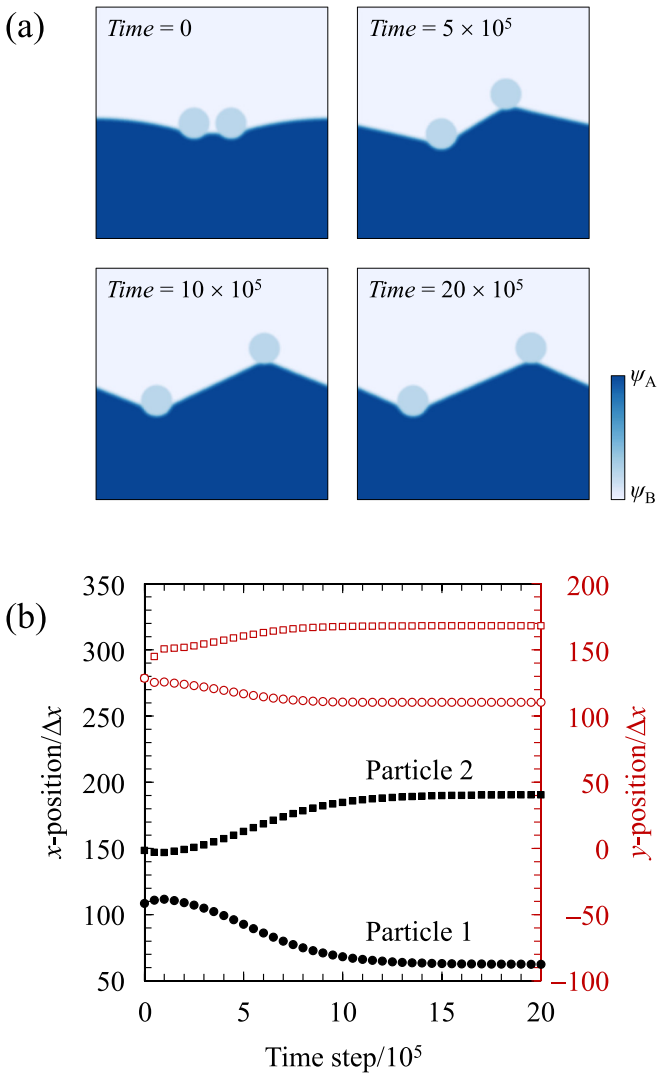

FIG. 8. Simulation results for system D.3 containing two similar particles with different mass densities of $\rho_{p,1} = 1.5\rho_f$ and $\rho_{p,2} = 0.5\rho_f$, which were initially placed at the same vertical position and separated by a horizontal center-to-center distance of $2\delta = 40\Delta x$ [e.g., Fig. 5(a)] and then allowed to move freely in all directions toward mechanically equilibrated positions [e.g., Fig. 5(c)]: (a) time-series snapshots and (b) the x and y positions (left- and right-hand-side axes) of particles 1 and 2 as a function of time.

As an additional demonstration of the proposed model, two freely moving particles with $\rho_{p,1} = 1.5\rho_f$ and $\rho_{p,2} = 0.5\rho_f$ at a fluid-fluid interface were simulated almost identically to the conditions described above: (i) particles separated by $2\delta = 40\Delta x$ were fixed at a flat fluid-fluid interface, (ii) the two-phase fluid around the fixed particles was allowed to flow to achieve the mechanically equilibrated state, and (iii) the particles were allowed to move freely in all directions. The simulation results are displayed in Fig. 8. At $t = 0$, the two particles stayed close to each other at the same level slightly below the fluid-fluid interface. The heavy-weight and the light-weight particles then moved downward and upward, respectively; they also moved horizontally in the opposite directions due to the repulsive capillary floatation force acting between them. The two particles were eventually located at their mechanically equilibrated positions. Therefore, the proposed model can provide stable and accurate simulations of particle dynamics at a fluid-fluid interface.

E. Capillary immersion force: Two vertically constrained particles at fluid-fluid interface

Let us consider system E in Table I, where two wettable particles trapped at a fluid-fluid interface are vertically constrained and move in the horizontal direction only. These two vertically constrained particles experience a capillary immersion force in the horizontal direction. Although system E is very similar to system D, as shown in Figs. 5(a)

and 5(b), it exhibits different phenomena. For example, when two particles are in direct contact with a solid plate covered with a thin film of phase A in a host fluid of phase B, the partially wetted particles can move in the horizontal direction only [2,3].

1. Theoretical description of system E

As shown in Figs. 5(a) and 5(b), for system E, two identical particles with a radius R and a contact angle α (i.e., wettability of χ) trapped at a fluid-fluid interface are separated by a horizontal center-to-center distance of 2δ and constrained at the same vertical position. In the mechanically equilibrated state, the resultant downward distance from the fluid-fluid interface to each particle center is represented by h, while the symbols of Ψ, Ψ', R_c, and ΔP are defined in the same fashion as for system D of two identical particles. Hence, the formal expressions for system E are the same as those for system D [e.g., Eqs. (51), (58), (60), (62), and (63)], except for several expressions described below.

The lateral force $F^{\rm lat}$ acting on each particle is given by Eq. (60), while Eq. (61) must be replaced with an equation for vertical force as follows:

$$F^{\rm ver} = \sigma(\sin\Psi + \sin\Psi') + R\left\{\cos\left(\frac{\pi}{2} - \alpha + \Psi\right) + \cos\left(\frac{\pi}{2} - \alpha + \Psi'\right)\right\}\Delta P, \tag{76}$$

where $F^{\rm ver} > 0$ and $F^{\rm ver} < 0$ represent the upward and downward forces on each particle, respectively. The pressure difference ΔP in Eqs. (60) and (76) is given by Eq. (51) with the following curvature radius:

$$R_c = \frac{h - R\cos(\alpha - \Psi)}{1 - \cos\Psi} = \frac{L - \delta - R\sin(\alpha - \Psi)}{\sin\Psi}, \tag{77}$$

which is obtained from Eqs. (58) and (62).

When $\Psi \neq 0$, the expansion of Eq. (77) leads to the following analytical expressions of Ψ and R_c:

$$\Psi = 2\tan^{-1}\left[\frac{\frac{h}{R} - \cos\alpha}{\frac{L-\delta}{R} + \sin\alpha}\right], \tag{78}$$

$$R_c = \frac{1+\tau^2}{2\tau^2}h - \left(\frac{1}{\tau}\sin\alpha + \frac{1-\tau^2}{2\tau^2}\cos\alpha\right)R = \frac{1+\tau^2}{2\tau}(L-\delta) - \left(\frac{1-\tau^2}{2\tau}\sin\alpha - \cos\alpha\right)R, \tag{79}$$

where $L/2 > \delta \geqslant R$ and $\tau \equiv \tan(\Psi/2)$ are employed. The values of Ψ and R_c are calculated using Eqs. (78) and (79), respectively, with the preset values of h as well as L, δ, R, and α. Subsequently, ΔP is calculated using Eq. (51). Finally, Eq. (63) results in Eq. (66), leading to

$$\Psi' = \sin^{-1}\left[\frac{-B \pm \sqrt{B^2 - AC}}{A}\right] \quad \text{for } R_c \gtrless 0, \tag{80}$$

with the calculated values of A, B, and C from Eq. (68). The lateral force $F^{\rm lat}$ and vertical force $F^{\rm ver}$ are then calculated using Eqs. (60) and (76), respectively. The condition for system stability is determined by considering the physically possible values of Ψ, R_c, and Ψ' in Eqs. (78)–(80) with Eq. (68) as follows:

$$\left|\frac{h}{R} - \cos\alpha\right| < \frac{L-\delta}{R} + \sin\alpha, \tag{81}$$

where $L/2 > \delta \geqslant R$.

When $\Psi = 0$, the expansion of Eq. (77) with Eqs. (51) and (63) leads to

$$\begin{aligned} h &= h_0 \equiv R\cos\alpha, \\ \Psi' &= 0, \\ 1/R_c &= 0, \\ \Delta P &= 0, \end{aligned} \tag{82}$$

where the wide- and narrow-gap fluid-fluid interfaces around the two vertically constrained particles are not deformed but horizontally flat.

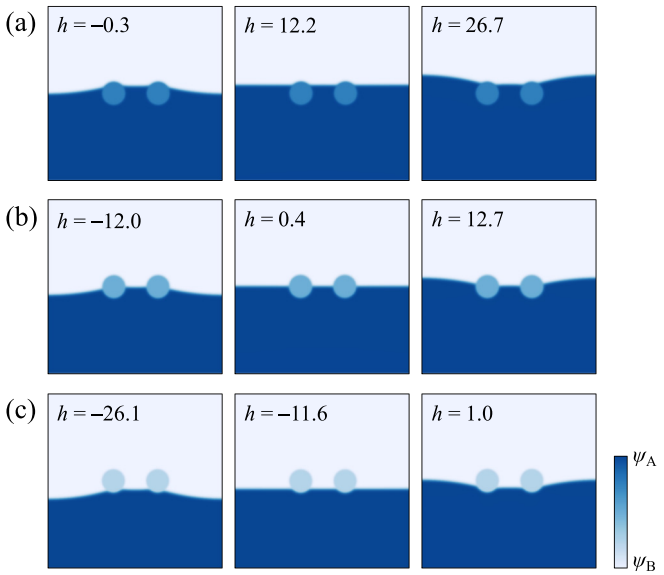

FIG. 9. Typical snapshots for the simulation of system E in a mechanically equilibrated state, corresponding to Fig. 5: (a) system E.1 with a contact angle of $\alpha = 45°$, (b) system E.2 with $\alpha = 90°$, and (c) system E.3 with $\alpha = 135°$, where two identical particles with a radius of $R = 16\Delta x$ were constrained at the same vertical position and separated by a horizontal center-to-center distance of $2\delta = 64\Delta x$ $(= 4R)$ throughout system E (see Table I). For every panel, from left to right, the snapshots obtained for downward distances of $h < h_0$, $h \approx h_0$, and $h > h_0$ are shown, where $h_0 \equiv R\cos\alpha$, corresponding to slope angles of $\Psi < 0°$, $\Psi \approx 0°$, and $\Psi > 0°$, respectively.

2. Simulations of system E

Simulations of system E were performed in the same way as those of system D, except for the following points. Two identical particles with a radius R and contact angle α were constrained at the same vertical position of the midline of the simulation cell and horizontally separated by a center-to-center distance of $2\delta = 64\Delta x$, where the area fraction of fluid phase A was set to the range of 0.43–0.57 (Table I), resulting in different downward distances h. The two-phase fluid around the two fixed particles was allowed to flow to achieve a

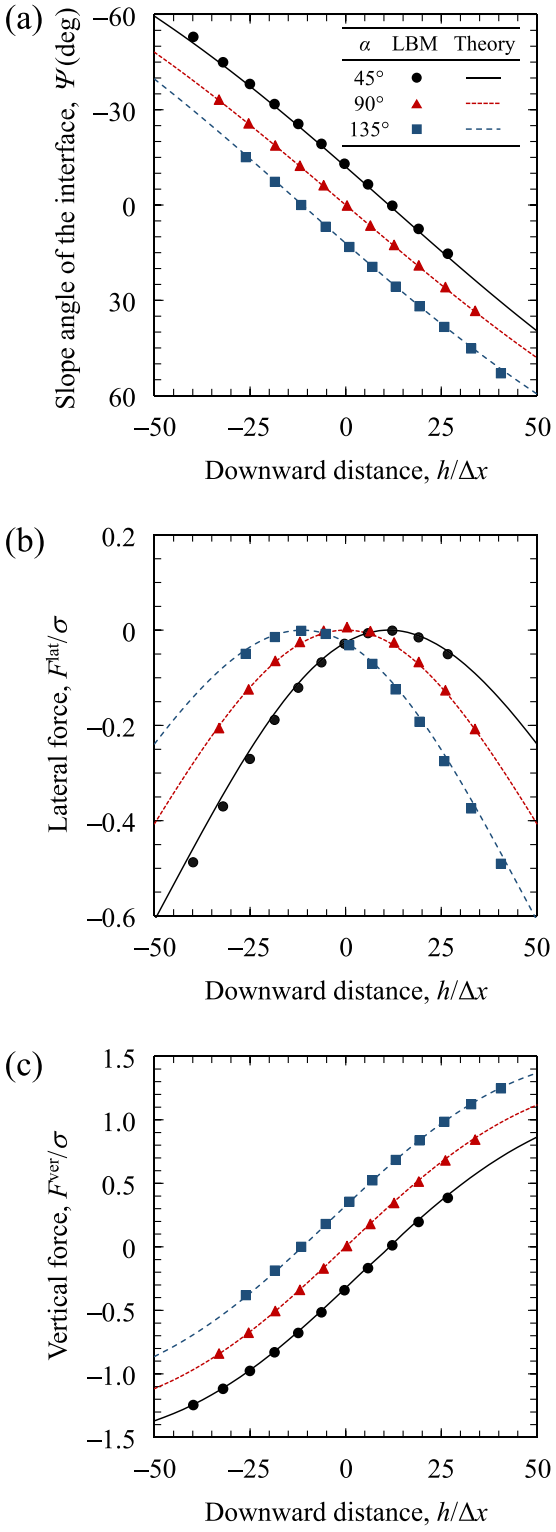

FIG. 10. Simulation results (filled symbols) and theoretical estimations (lines) of system E (see Table I) in a mechanically equilibrated state, which are similar to parts (a) and (b) of Figs. 5 and 6, where two identical particles constrained at the same vertical position and separated by a horizontal center-to-center distance of $2\delta = 64\Delta x$ are trapped at a deformed fluid-fluid interface in the absence of gravity, experiencing not only a capillary immersion force in the horizontal direction but also a vertical force depending on their downward distance h. (a) The slope angle of the fluid-fluid interface Ψ as a function of h, (b) capillary immersion force $F^{\rm lat}$ between the two particles as a function of h, and (c) vertical force $F^{\rm ver}$ as a function of h, where different contact angles of $\alpha = 45^\circ$, 90°, and 135° were considered. The lines in panels (a)–(c) represent the theoretical estimations from Eqs. (78), (60), and (76), respectively.

mechanically equilibrated state, as shown in Fig. 9. Regardless of the contact angles α, the wide- and narrow-gap fluid-fluid interfaces around the two particles were horizontally flat (i.e., $\Psi \approx 0^\circ$ and $\Psi' \approx 0^\circ$) for the values of $h \approx h_0 \equiv R\cos\alpha = 11.3\Delta x, 0$, and $-11.3\Delta x$ for $\alpha = 45^\circ$, 90°, and 135°, respectively. The fluid-fluid interfaces were deformed to be concave upward and downward for other values of $h < h_0$ (i.e., lower level of fluid phase A) and $h > h_0$ (i.e., higher level of fluid phase A), respectively. The slope angle Ψ as a function of h is presented in Fig. 10(a), demonstrating that the simulation results exactly coincide with the theoretical estimations.

The capillary immersion force $F^{\rm lat}$ and vertical force $F^{\rm ver}$ are displayed as a function of h in Figs. 10(b) and 10(c), respectively. Both $F^{\rm lat}$ and $F^{\rm ver}$ were almost zero at $h \approx h_0$, where $\Psi \approx 0^\circ$ and $\Psi' \approx 0^\circ$. Note that the first and second terms on the right-hand sides of Eqs. (60) and (76) originate from the interfacial tension σ and pressure difference ΔP, respectively. In the case of flat fluid-fluid interfaces (i.e., $\Psi = \Psi' = 0^\circ$), both the terms equal zero based on Eq. (82). In the other cases of $h < h_0$ and $h > h_0$, $F^{\rm lat}$ exhibits attractive forces, increasing with an increase in $|h - h_0|$, whereas $F^{\rm ver}$ exhibits downward and upward forces at the lower ($h < h_0$) and higher levels ($h > h_0$) of fluid phase A, respectively, also increasing with an increase in $|h - h_0|$. The simulation results for $F^{\rm lat}$ and $F^{\rm ver}$ agree with the theoretical estimations, similar to the case of Ψ.

IV. CONCLUSION

We developed a computational method for the simulation of wettable particles trapped at a fluid-fluid interface under gravity. The proposed method combines the iSP-LBM and the free-energy LBM for isodensity two-phase fluid flows. To test the performance of the proposed technique, we examined five benchmark problems in two-dimensional systems containing particles with various wettability: A, a stationary drop; B and C, a wettable particle trapped at a fluid-fluid interface in the absence or presence of gravity; D, two freely moving particles at a fluid-fluid interface in the presence of gravity (i.e., capillary floatation forces); and E, two vertically constrained particles at a fluid-fluid interface (i.e., capillary immersion forces).

The capillary floatation force between two particles was attractive for identical particle pairs with heavy-weight or light-weight but repulsive for the heavy- and light-weight particles. With a decrease in the separation distance between the particles, the fluid-fluid interface around the particles became more distorted, resulting in a stronger lateral force. The capillary immersion force was attractive and increased with an increase in curvature of the fluid-fluid interfaces. These simulation results are in quantitative agreement with theoretical estimations, indicating that the proposed method can reproduce the capillary interactions between wettable particles at a fluid-fluid interface under gravity. Nonetheless, further

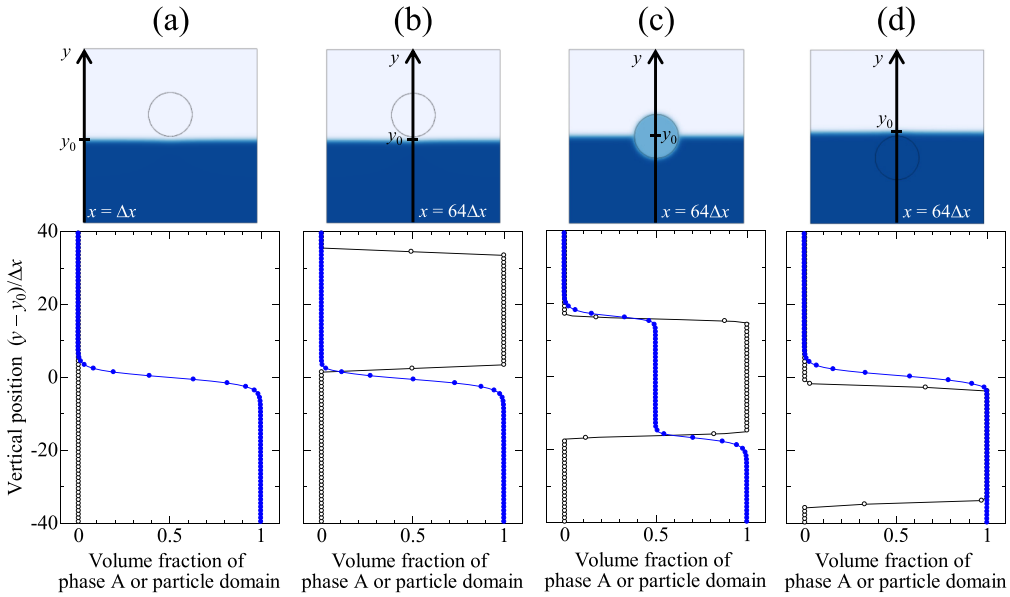

FIG. 11. Volume fractions of phase A (filled symbols) and particle domain (open symbols) as a function of vertical position, $y - y_0$, along the lines of $x = \Delta x$ for system B of $\chi = -1$ (a) and $x = 64\Delta x$ for system B of $\chi = -1$ (b), $\chi = 0$ (c), and $\chi = 1$ (d) (see Table I), where $y = y_0$ ($= 61.5\Delta x$, $64.8\Delta x$, and $67.8\Delta x$ for $\chi = -1$, 0, and 1, respectively) represents the level of a fluid-fluid interface. Every solid line is to guide the eyes.

examination is necessary to reduce the discrepancy between the simulation and theoretical results which appears when the particles approach each other. This will be addressed with the improvement of the proposed model in our future work.

ACKNOWLEDGMENTS

This work was financially supported in part by the Ministry of Education, Culture, Sports, Science and Technology in Japan (Grants-in-Aid for Scientific Research, Grant No. 18H03690), Hosokawa Powder Technology Foundation, and the Information Center of Particle Technology, Japan.

APPENDIX

Let us consider system B of $\chi = -1$, 0, and 1 to investigate the local composition of immiscible two phases around a particle trapped at a fluid-fluid interface in the absence of gravity. Figure 11 displays the volume fraction of phase A and particle domain as a function of vertical position y along the lines of $x = \Delta x$ and $64\Delta x$. As shown in Fig. 11(a), the fluid-fluid interface had a width of $\sim 10\Delta x$, which is thick enough to resolve the interface for accurate calculation of its interfacial tension. Figures 11(b)–11(d) demonstrate that every particle was successfully represented by both the particle-side domain with a diameter of $\sim 32\Delta x$ ($= 2R$) and a diffuse interface with a width of $\sim 2\Delta x$, as enforced by the SP function of Eqs. (6) and (7). Additionally, the volume fraction of phase A inside every wettable particle became almost constant, as constrained by the modified free energy of Eq. (35).

The solid-fluid interface around a circular particle in the present simulations was diffuse other than sharp to have a finite width of $\sim 2\Delta x$, whereas a physically sharp solid-fluid interface with zero width is assumed in Eq. (49) [34]. This explains the reason why agreement between the simulation results and the theoretical estimation in Fig. 3(b) became poorer with increasing affinity in magnitude. This discrepancy is estimated as ξ/R ($= 0.125$ in the present simulations), and could be diminished by using the large value of particle radius R with the small value of interface width ξ ($= 2\Delta x$).

[1] N. Bowden, A. Terfort, J. Carbeck, and G. M. Whitesides, Self-assembly of mesoscale objects into ordered two-dimensional arrays, Science **276**, 233 (1997).

[2] P. A. Kralchevsky and K. Nagayama, Capillary forces between colloidal particles, Langmuir **10**, 23 (1994).

[3] P. A. Kralchevsky and K. Nagayama, Capillary interactions between particles bound to interfaces, liquid films and biomembranes, Adv. Colloid Interface Sci. **85**, 145 (2000).

[4] P. J. Yunker, T. Still, M. A. Lohr, and A. G. Yodh, Suppression of the coffee-ring effect by shape-dependent capillary interactions, Nature (London) **476**, 308 (2011).

[5] E. Koos and N. Willenbacher, Capillary forces in suspension rheology, Science **331**, 897 (2011).

[6] A. J. C. Ladd, Numerical simulations of particulate suspensions via a discretized Boltzmann equation. Part 1. Theoretical foundation, J. Fluid Mech. **271**, 285 (1994).

[7] P. Lallemand and L. S. Luo, Lattice Boltzmann method for moving boundaries, J. Comput. Phys. **184**, 406 (2003).

[8] Z. G. Feng and E. E. Michaelides, The immersed boundary-lattice Boltzmann method for solving fluid–particles interaction problems, J. Comput. Phys. **195**, 602 (2004).

[9] X. D. Niu, C. Shu, Y. T. Chew, and Y. Peng, A momentum exchange-based immersed boundary-lattice Boltzmann method for simulating incompressible viscous flows, Phys. Lett. A **354**, 173 (2006).

[10] J. Wu and C. Shu, Implicit velocity correction-based immersed boundary-lattice Boltzmann method and its applications, J. Comput. Phys. **228**, 1963 (2009).

[11] A. K. Gunstensen, D. H. Rothman, S. Zaleski, and G. Zanetti, Lattice Boltzmann model of immiscible fluids, Phys. Rev. A **43**, 4320 (1991).

[12] D. Grunau, S. Chen, and K. Eggert, A lattice Boltzmann model for multiphase fluid flows, Phys. Fluids A **5**, 2557 (1993).

[13] X. Shan and H. Chen, Lattice Boltzmann model for simulating flows with multiple phases and components, Phys. Rev. E **47**, 1815 (1993).

[14] G. Falcucci, G. Bella, G. Chiatti, S. Chibbaro, M. Sbragaglia, and S. Succi, Lattice Boltzmann models with mid-range interactions, Commun. Comput. Phys. **2**, 1071 (2007).

[15] M. R. Swift, W. R. Osborn, and J. M. Yeomans, Lattice Boltzmann Simulation of Nonideal Fluids, Phys. Rev. Lett. **75**, 830 (1995).

[16] M. R. Swift, E. Orlandini, W. R. Osborn, and J. M. Yeomans, Lattice Boltzmann simulations of liquid-gas and binary fluid systems, Phys. Rev. E **54**, 5041, (1996).

[17] S. Succi, *The Lattice Boltzmann Equation for Fluid Dynamics and Beyond* (Oxford University Press, Oxford, 2001).

[18] S. Chen and G. D. Doolen, Lattice Boltzmann method for fluid flows, Annu. Rev. Fluid Mech. **30**, 329 (1998).

[19] J. Onishi, A. Kawasaki, Y. Chen, and H. Ohashi, Lattice Boltzmann simulation of capillary interactions among colloidal particles, Comput. Math. Appl. **55**, 1541 (2008).

[20] A. S. Joshi and Y. Sun, Multiphase lattice Boltzmann method for particle suspensions, Phys. Rev. E **79**, 066703 (2009).

[21] J. Y. Shao, C. Shu, and Y. T. Chew, Development of an immersed boundary-phase field-lattice Boltzmann method for Neumann boundary condition to study contact line dynamics, J. Comput. Phys. **234**, 8 (2013).

[22] K. W. Connington, T. Lee, and J. F. Morris, Interaction of fluid interfaces with immersed solid particles using the lattice Boltzmann method for liquid–gas–particle systems, J. Comput. Phys. **283**, 453 (2015).

[23] S. Jafari, R. Yamamoto, and M. Rahnama, Lattice-Boltzmann method combined with smoothed-profile method for particulate suspensions, Phys. Rev. E **83**, 026702 (2011).

[24] Y. Mino, H. Shinto, S. Sakai, and H. Matsuyama, Effect of internal mass in the lattice Boltzmann simulation of moving solid bodies by the smoothed-profile method, Phys. Rev. E **95**, 043309 (2017).

[25] T. Inamuro, T. Ogata, S. Tajima, and N. Konishi, A lattice Boltzmann method for incompressible two-phase flows with large density differences, J. Comput. Phys. **198**, 628 (2004).

[26] T. Lee and C. L. Lin, A stable discretization of the lattice Boltzmann equation for simulation of incompressible two-phase flows at high density ratio, J. Comput. Phys. **206**, 16 (2005).

[27] A. Mazloomi M, S. S. Chikatamarla, and I. V. Karlin, Entropic Lattice Boltzmann Method for Multiphase Flows, Phys. Rev. Lett **114**, 174502 (2015).

[28] T. Inamuro, R. Tomita, and F. Ogino, Lattice Boltzmann simulations of drop deformation and breakup in shear flows, Int. J. Mod. Phys. B **17**, 21 (2003).

[29] Y. Nakayama and R. Yamamoto, Simulation method to resolve hydrodynamic interactions in colloidal dispersions, Phys. Rev. E **71**, 036707 (2005).

[30] Y. Nakayama, K. Kim, and R. Yamamoto, Simulating (electro) hydrodynamic effects in colloidal dispersions: Smoothed profile method, Eur. Phys. J. E **26**, 361 (2008).

[31] T. Inamuro, Lattice Boltzmann methods for moving boundary flows, Fluid Dyn. Res. **44**, 024001 (2012).

[32] H. Shinto, Computer simulation of wetting, capillary forces, and particle-stabilized emulsions: From molecular-scale to mesoscale modeling, Adv. Powder Technol. **23**, 538 (2012).

[33] G. Falcucci, S. Ubertini, D. Chiappini, and S. Succi, Modern lattice Boltzmann methods for multiphase microflows, IMA J. Appl. Math. **76**, 712 (2011).

[34] D. Iwahara, H. Shinto, M. Miyahara, and K. Higashitani, Liquid drops on homogeneous and chemically heterogeneous surfaces: A two-dimensional lattice Boltzmann study, Langmuir **19**, 9086 (2003).

[35] P. C. Millett and Y. U. Wang, Diffuse-interface field approach to modeling arbitrarily-shaped particles at fluid–fluid interfaces, J. Colloid Interface Sci. **353**, 46 (2011).